Spin disorder and magnetic anisotropy in Fe_3O_4 nanoparticles

E. Lima, Jr., A. L. Brandl, A. D. Arelaro, and G. F. Goya[a)]
Instituto de Física, Universidade de São Paulo, CP 66318, 05315-970 São Paulo, Brazil

(Received 28 November 2005; accepted 6 March 2006; published online 4 May 2006)

We have studied the magnetic behavior of dextran-coated magnetite (Fe_3O_4) nanoparticles with median particle size $\langle d\rangle = 8$ nm. Magnetization curves and in-field Mössbauer spectroscopy measurements showed that the magnetic moment M_S of the particles was much smaller than the bulk material. However, we found no evidence of magnetic irreversibility or nonsaturating behavior at high fields, usually associated to spin canting. The values of magnetic anisotropy K_{eff} from different techniques indicate that surface or shape contributions are negligible. It is proposed that these particles have bulklike ferromagnetic structure with ordered A and B sublattices, but nearly compensated the magnetic moments. The dependence of the blocking temperature with frequency and applied fields, $T_B(H,\omega)$, suggests that the observed nonmonotonic behavior is governed by the strength of interparticle interactions. © *2006 American Institute of Physics*.
[DOI: 10.1063/1.2191471]

I. INTRODUCTION

Iron oxide nanoparticles have gained technological significance after they became known as media contrast agents in clinical protocols for magnetic resonance imaging (MRI) and magnetic fluid hyperthermia (MFH). For these applications, magnetite (Fe_3O_4) and maghemite (γ-Fe_2O_3) nanoparticles are the preferred phases because of their low toxicity, high saturation magnetic moment at room temperature ($M_S \sim 75$ and 82 emu/g, respectively) and the highest ordering temperatures among spinel ferrites.[1] To improve stability and biocompatibility the particles are coated with a polysaccharide and suspended in water-based solvents. Despite the success attained in obtaining efficient dispersions of iron oxide particles for the MRI protocols, the understanding of the effects of these coatings on the efficacy in MRI or MFH applications (from which a material with desired properties can be designed for specific purposes) is far from complete.[2–5]

Regarding the fundamental mechanisms that govern the magnetic behavior of a magnetic colloid, the connection between single-particle properties and collective behavior of the *ensemble* of magnetic nanoparticles has many subtle facets. When entering the few-nanometer scale the magnetic behavior of a single particle gradually differs from the corresponding bulk materials, making increasingly inaccurate the description of the collective behavior in terms of "bulklike" entities. Dipolar magnetic interactions between ferromagnetic nanoparticles are known to affect the magnetic dynamics of the system through changes on the average anisotropy energy barriers, which in turn determines the relaxation times, magnetic hardness, and ordering temperature. Indeed, the effects of interparticle interactions are not restricted only to the anisotropy barriers but have also been proposed as stabilizers of the magnetic order at both particle core and surface.[6] In spite of the sustained efforts to solve this problem along the last decade, the exact mechanisms linking these properties are still being discussed.[7,8] Theoretical approaches usually start from the original model proposed by Stoner and Wolfarth[9] for noninteracting, monodispersed single-domain particles, and add some specific perturbation to the collective or single-particle properties within different mathematical landscapes. In this way microscopic mechanisms such as spin disorder, surface contributions, and collective behavior for strongly correlated particles have been added to the original model.[10–12] On the other side, suitable experimental systems for testing those models are still a key problem to be solved, because of the difficulty of synthesizing samples with different (controlled) particle size distribution and particle interactions.[13–15]

Magnetite is a mixed (Fe^{2+} and Fe^{3+}) iron oxide with spinel structure, composed by a cubic close packed oxygen array, plus six (2+4) interpenetrating fcc lattices of two nonequivalent cation sites with fourfold ($8a$) and sixfold ($16d$) oxygen coordination, labeled as A and B sites, respectively. The cubic unit cell has lattice parameter $a = 8.39$ Å.[16] Magnetic interactions within A and B sublattices are of ferromagnetic type, whereas the strong antiferromagnetic A-B coupling yields a high Curie temperature $T_C = 850$ K. Bulk Fe_3O_4 is magnetically soft, i.e., the magnetization can be fully saturated in fields $H \lesssim 1$ kOe for any crystal direction.[17] At room temperature, the combination of first- and second-order magnetocrystalline anisotropy constants $K_1 = -13 \times 10^4$ erg/cm^3 and $K_2 = -3 \times 10^4$ erg/cm^3 makes the easy axis of magnetization to be along the crystallographic [111] direction.[18] At low temperatures magnetite undergoes a first-order transition, namely, the Verwey transition, located at $T_V \sim 115-124$ K depending on sample conditions.[19] The most conspicuous evidence of this transition is the sharp increase of the resistivity by two orders of magnitude,[19,20] but also other properties such as magnetization, thermopower, and reflectivity show abrupt changes. Regarding the structural transition reported at T_V, there is some consensus about the ortorhombic symmetry of the low-T phase, but no conclusive structural model has yet emerged.[21,22] Despite the

[a)]Present address: Instituto de Nanociencia de Aragón, Universidad de Zaragoza, Zaragoza, Spain; electronic mail: goya@unizar.es

different crystal structures proposed for the low temperature phase, magnetic measurements have shown that below T_V the magnetocrystalline anisotropy energy can be described as having orthorhombic symmetry with the easy c axis tilted $\sim 0.2^\circ$ from the $\langle 100 \rangle$ cubic axis, and the a (hard) and b axes lying on the former cubic (001) plane.[23] The resulting anisotropy is then uniaxial with constants $K_a \approx 2 \times 10^6$ erg/cm^3 and $K_b = 21 \times 10^4$ erg/cm^3, considerably larger than the K_1 constant of the high-T phase.[24,25]

In this work we performed a detailed magnetic and structural characterization of a colloidal suspension of dextran-coated magnetite nanoparticles, with the purpose of systematically characterize both the single-particle properties and the resulting collective behavior. The present paper is organized as follows: in Sec. II, the experimental procedures are described. In Sec. III the results are presented and discussed in four parts; Sec. III A deals with the analysis of the structural data. In Sec. III B the results from magnetization measurements are shown. Section III C describes the Mössbauer data obtained with different applied fields and temperatures. Finally, the discussion and conclusions drawn from the present work are given in Sec. IV.

II. EXPERIMENTAL PROCEDURE

The samples studied in this work consisted of dextran-coated magnetite nanoparticles dispersed in a water-based ferrofluid (ENDOREM™, Guerbet) used in clinical protocols as a contrast agent for magnetic resonance imaging of the liver and the spleen.[26] The dispersion of nanoparticles was studied *as supplied*, i.e., suspended in an aqueous liquid carrier, conditioned in sealed cylindrical sample holders (5 mm diam × 6 mm high). A second fraction of the sample was lyophilized (@$T = 85$ K and $P = 10^{-4}$ Torr) to increase the particle concentration keeping the particle size distribution unaltered. These as supplied and lyophilized samples will be labeled hereafter as END1 and ENDS, respectively. Characterization through x-ray diffraction (XRD) was performed in a Philips PW 1820 diffractometer using Cu $K\alpha$ radiation ($\lambda = 1.5418$ Å) and Ni filter. Transmission electron microscopy (TEM) images were performed using a 200 kV Model CM200 Philips electron microscope, conditioning the samples by dropping an alcohol-powder suspension on a carbon-coated nickel grid. The elemental analysis of carbon, hydrogen, nitrogen, and sulphur contents was performed with a Perkin-Elmer 2400 CHNS microanalyzer. The Mössbauer spectroscopy (MS) measurements were performed between 4.2 and 296 K in a liquid He flow cryostat, with a conventional constant-acceleration spectrometer in transmission geometry using a ^{57}Co/Rh source with c.a. 50 mCi activity. For the in-field Mössbauer measurements, the powder samples were prepared between acrylic disks, and mounted in the bore of a 140 kOe superconducting magnet, in a vertical source-sample-detector setup such that the direction of gamma ray propagation was parallel to the magnetic-field axis. For this setup, a sine-shaped velocity waveform was used to minimize mechanical noise. The spectra were fitted to Lorentzian line shapes using a nonlinear least-squares program, calibrating the velocity scale with a foil of α-Fe at 296 K. When necessary, a distribution of hyperfine magnetic fields, isomer shift, and quadrupole splitting have been used to fit the spectra. Magnetization and ac magnetic susceptibility measurements were performed in a commercial superconducting quantum interferometer device (SQUID) magnetometer both in zero-field-cooling (ZFC) and field-cooling (FC) modes, between $1.8\ \text{K} < T < 250$ K and under applied fields up to $H = 70$ kOe. The frequency dependence of both in-phase $\chi'(T)$ and out-of-phase $\chi''(T)$ components of the ac magnetic susceptibility were measured by using excitation fields of 1–4 Oe and driving frequencies $0.01\ \text{Hz} \leqslant f \leqslant 1500$ Hz.

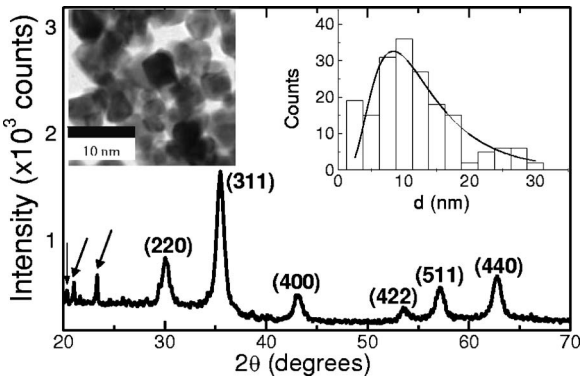

FIG. 1. Powder x-ray-diffraction profile of the lyophilized sample ENDS indexed with the (hkl) reflections of the cubic Fe_3O_4 phase. The arrows correspond to organic materials. Upper left panel: selected-area from TEM images of Fe_3O_4 nanoparticles where some surface faceting is observable. Upper right panel: histogram of the particle size populations as observed from TEM images. The solid line is the best fit using a log-normal distribution with $\langle d \rangle_{\text{TEM}} = 8.3 \pm 0.8$ nm and $\sigma_d = 0.6$.

III. EXPERIMENTAL RESULTS

A. Structural analysis

The XRD profile of the lyophilized powder (Fig. 1) was composed of broad lines that could be indexed with a cubic spinel crystal structure. The presence of minor amounts of unknown organic ingredients (used for coating and stabilizing the ferrofluid) were also detected. A rough estimation of the average grain size $\langle d \rangle_{RX} = 7 \pm 1$ nm was obtained by applying the Scherrer formula to the most intense XRD line of the spinel structure, without including the effects from crystal stress. This is in agreement with previously reported low temperature Mössbauer data[27,28] that showed the existence of Fe_3O_4 as the only phase, without evidences of the related γ-Fe_2O_3 (maghemite) or α-Fe_2O_3 (hematite) phases.

Figure 1 also shows the particle size histogram obtained by measuring the diameter of about 200 particles in transmission electron microscopy (TEM) images. The resulting histogram could be fitted with a log-normal distribution, with median diameter $\langle d \rangle_{\text{TEM}} = 8.3 \pm 0.8$ nm and distribution width $\sigma_d = 0.6$. It can be noticed from comparison between the fitted curve and the experimental histogram that the counted number of particles with $d < 3$ nm is considerably larger than the expected from a pure log-normal size distribution with the fitted parameters. The magnified TEM image of specific areas showed particles with spherical-like shapes, although for few particles with the largest diameters we observed fac-

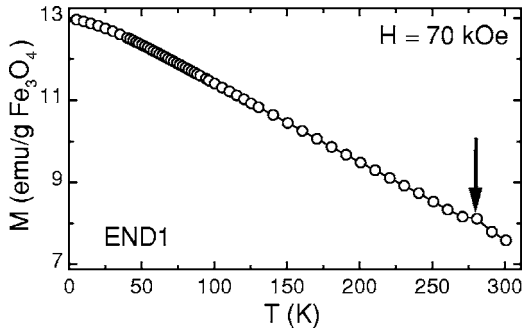

FIG. 2. Magnetization curve of END1 sample after field cooling (H_{FC} =70 kOe) from 300 K, and measured for increasing T values at the same field. The arrow indicates the melting point of the frozen suspension.

eted particles, as selected in the inset of Fig. 1. The latter shape is probably related to the high crystallinity of the particles reflecting the cubic crystal habit of the Fe_3O_4 phase.

B. Magnetization data

Some of the basic magnetic features of the present particles established previously[27,28] are summarized here for clarity.[29] The particles were superparamagnetic (SPM) at room temperature, and magnetization curves $M(T)$ taken in FC and ZFC modes showed blocking temperatures T_B of ca. 50 K (for H=100 Oe).[27] Additionally, the ac susceptibility data $\chi(T,f)$ confirmed[28] the thermally activated (Arrhenius) nature of the blocking process, and indicated that the effect of interparticle interactions was to increase the energy barriers.

In order to measure the evolution of the saturation magnetization of the particles with temperature, we applied a field of H=70 kOe at T=300 K (i.e., above the melting temperature of the liquid carrier) to the *as provided* sample, cooled down the system and measured the $M_{FC}(T)$ curve for increasing temperatures keeping the same field. It can be seen from Fig. 2 that these fully aligned particles show a nearly linear dependence of the $M_{FC}(T)$ data, varying within $\approx$13–7 emu/g in the $1.8 \leqslant T \leqslant 300$ K temperature range. All magnetization values were converted into emu/g Fe_3O_4 units by subtracting the mass of organic components as determined from elemental CHNS analysis, calibrated within 0.1% precision (Table I). These results were in agreement with the expected nanoparticle concentration from the nominal composition of the ferrofluid (0.07 mol Fe_3O_4/l) and yielded saturation values M_S=10–12 emu/g, much smaller than the expected 85–95 emu/g for bulk magnetite. Additionally, the $M(T)$ curves did not show any indication of the jump in the magnetization expected for the Verwey transition.[19] To explore possible aging (oxidation) effects we

TABLE I. Sample composition obtained from CHNS elemental analysis of carbon, hydrogen, nitrogen, and sulphur contents. The (NP) column is the calculated particle concentration (in particle/cm^3).

Sample	H (%)	C (%)	N (%)	S (%)	(NP)
END1	60.3(5)	26.4(5)	3.3(5)	1.1(5)	6.5×10^{15}
ENDS	2.0(5)	24.2(5)	0.8(5)	0.0(5)	1.6×10^{17}

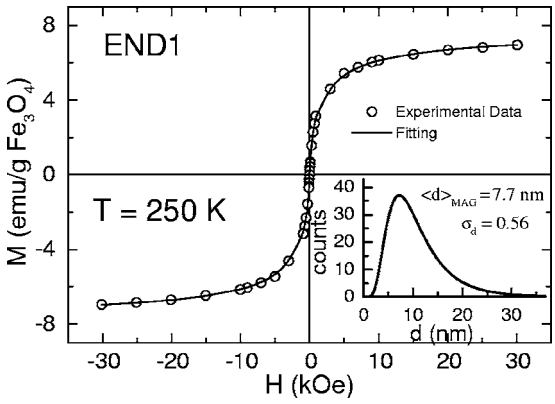

FIG. 3. Fit of $M(H,250\ \text{K})$ curve for sample END1 using Eq. (1). The values of $\bar{\mu}$ and σ_μ obtained for the best fit are $290\mu_B$ and 1.68, respectively.

compared our initial measurements with other runs performed after several months, taken in three different magnetometers, finding that the magnetic moment was reproduced within a few percent of precision. Additional support for the observed reduction of the magnetic moment of the particles came from the $M(H)$ curves both below and above the blocked temperature $T_B \approx 40$ K (see below). As will be discussed in Sec. III C, the Mössbauer data showed no indication of other iron oxides of smaller magnetic moment, as could be expected in case of particle oxidation (hematite Fe_2O_3) or hydration (ferrihydrite). Therefore we attempted to verify these rather low values by independent measurements, namely, the magnetic behavior in the SPM state.

The magnetization $M_{SPM}(H,T)$ of an ensemble of noninteracting, single-domain particles in the SPM state, each with magnetic moment μ, can be represented by a Langevin function $L(x)$ of argument $x=\mu H/k_BT$. Therefore all data $M(H,T)$ should scale into a single curve when plotted against H/T, provided that $T_B \ll T \ll T_C$. Based on the log-normal distribution of particle sizes obtained from TEM data, we modify the model above by using a distribution-weighted sum of the Langevin functions[30]

$$M_{SPM} = N\int_0^\infty \mu L\left(\frac{\mu H}{k_B T}\right) f(\mu)\, d\mu, \tag{1}$$

where $f(\mu)$ is the log-normal distribution function

$$f(\mu) = \frac{1}{\sqrt{2\pi}\sigma_\mu \mu} \exp\left\{-\frac{\ln^2[\mu/\langle\mu\rangle]}{2\sigma_\mu^2}\right\} \tag{2}$$

of magnetic moments μ. In this equation σ_μ is the distribution width and $\langle\mu\rangle$ is the median of the distribution related to the mean magnetic moment μ_m by $\mu_m = \langle\mu\rangle \exp(\sigma_\mu^2/2)$.[30]

The best fit for sample END1 (for which dipolar interactions are expected to be less important) yielded a median magnetic moment $\langle\mu\rangle = 290\mu_B$ and a distribution width σ_μ =1.68 for the highest measured temperature (see Fig. 3). The fittings of $M(H)$ curves were performed for T=100, 150, 200, and 250 K. We have observed that the resulting median value $\langle\mu\rangle$ increased ca 10% from 250 to 100 K, which is likely to be related to the temperature dependence of the magnetic moment $M(T)$ discussed above (Fig. 2). The distribution width σ_μ decreased $\approx$6% within the same tempera-

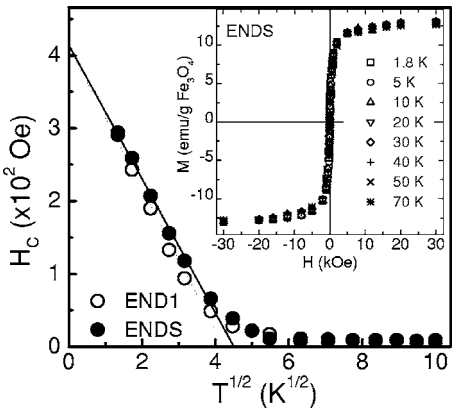

FIG. 4. Temperature dependence of the coercive field $H_C(T)$ extracted from $M(T,H)$ cycles. The solid lines represents the linear fits using Eq. (3) for samples ENDS and END1. The inset shows typical magnetization curves $M(H,T)$ for lyophilized sample ENDS taken at different temperatures. Note that $M(H)$ approaches to saturation for fields $H \gtrsim 10$ kOe.

ture range. To relate this moment distribution to a particle size distribution we have assumed spherical geometry for the particles, as observed from TEM data [i.e., $\langle\mu\rangle = M_S(\pi/6) \times \langle d\rangle^3$] and the *experimental* saturation magnetization value $M_S = 7.2$ emu/g from the $M(H)$ data at the same temperature. We have obtained $\langle d\rangle_{\mathrm{MAG}} = 7.7 \pm 0.5$ nm with $\sigma_d = 0.56$. The median particle size $\langle d\rangle_{\mathrm{MAG}}$ obtained with the measured M_S value is in close agreement with the $\langle d\rangle_{\mathrm{TEM}} = 8.3 \pm 0.8$ nm from the TEM micrographs, and the corresponding distribution widths are identical within experimental accuracy. The outsized reduction in the magnetic moment of the particles observed in $M(T)$ curves (Fig. 2) in the blocked state is therefore supported, independently, by the measured $M(H,T)$ curves in the SPM state. The origin of this reduction will be discussed in Sec. IV. We note here that the latter procedure for obtaining the particle magnetic moment $\bar{\mu}$ does not depend on the absolute magnetization values but on the μH product for a given temperature.

We have further characterized the transition from blocked to SPM state by measuring the hysteresis curves $M(H)$ at different temperatures between 1.8 and 100 K for samples END1 and ENDS. From the obtained $M(H,T)$ curves (Fig. 4) it is observed that the coercivity fields H_C of both samples remain essentially zero down to $T \approx 17-18$ K, increasing appreciably below this temperature. The temperature dependence of $H_C(T)$, as extracted from $M(H,T)$ curves, is the expected for single-domain particles, i.e.,

$$H_C = H_{C0}\left[1 - \left(\frac{25 k_B T}{K_{\mathrm{eff}} V}\right)^{1/2}\right], \tag{3}$$

where $H_{C0} = 2\alpha K_{\mathrm{eff}}/M_S$, and $\alpha = 0.48$ is a phenomenological constant used for a randomly oriented distribution of easy axis.[9]

Therefore, Eq. (3) can be used for determining K_{eff} from the slope of the $H_C(T)$ curves, through the product $E_a = K_{\mathrm{eff}} V$, using the extrapolated value H_{C0}. Expressing E_a in terms of an anisotropy field $E_a = H_K M_S$, the effective anisotropy constant K_{eff} for a cubic system with easy axis along the [111] direction is related to K_1 and K_2 through $K_{\mathrm{eff}} = \frac{4}{3}K_1 + \frac{4}{9}K_2$,[31] and thus $K_{\mathrm{eff}} = 18.7 \times 10^4$ erg/cm^3 for bulk Fe_3O_4. The values of K_{eff} were extracted from the best fit of Eq. (3) for $T \leqslant 15$ K, and the calculation was made using *both* the mean value from TEM distribution $\langle d\rangle = 8.3$ nm and the experimental $M_S = 12$ emu/g values from the $M(H)$ data at low temperatures. The resulting K_{eff} values shown in Table II are very close to the expected anisotropy of bulk magnetite, suggesting that no major contributions other than magnetocrystalline are important. These values are also in agreement with our previous results obtained from the low temperature Mössbauer data.[28] By extrapolating the linear fits to $H_C(T) = 0$, we found values of $T_B = 17.4$ K and 18.5 K for samples END1 and ENDS, respectively. We mention that these values obtained from the extrapolation of $H_C(T)$ are smaller than the blocking temperatures obtained from ZFC curves, which we associate to the different field regimes of each measurement (see discussion in Sec. IV). The extrapolated $T \to 0$ K values were $H_{C0} = 418$ Oe and 428 Oe for samples END1 and ENDS, respectively. It is worth noting from Fig. 4 that the saturation of the magnetization ($M \geqslant 0.95 M_S$) is attained for $H \approx 10$ kOe, the value of M_S being calculated from the $H^{-1} \to 0$ extrapolation in the M vs H^{-1} curves. These saturating fields are low when compared with results from other nanoparticles of similar average sizes, where nonsaturating behavior extended for applied fields larger than 70–90 kOe.[32–34] For sample END1 the extrapolated $M_S = 13.5$ emu/g value from the $M(H)$ curves at $T = 1.8$ K (Fig. 4) is slightly larger than the $M_S = 12.9$ emu/g value from FC data (Fig. 2). The origin of this difference is probably related to differences in particle alignment when the field is applied in the liquid state (FC process) and below the blocking temperature [$M(H)$ curves].

TABLE II. Median particle diameter $\langle d\rangle$, effective anisotropy constant K_{eff} and energy barrier E_a/k_B obtained from thermal dependence of coercive field [$H_C(T)$]; the Langevin fits of the SPM magnetization (M_{SPM}); thermal dependence of the hyperfine fields [Eq. (6)].

	$\langle d\rangle$ (nm)[a]		K_{eff} (10^4 erg/cm^3)[b]		E_a/k_B (K)	
	END1	ENDS	END1	ENDS	END1	ENDS
$H_C(T)$	8.6	9.0	20.7	23.5	449	509
M_{SPM}	7.7[c]	7.9[c]	⋯	⋯	323[a]	349[a]
Moss	⋯	9.1	⋯	24.3	⋯	526
$\chi_{ac}(f,T)$[d]	9.9	10.3	32.1	35.1	694	763

[a]Values calculated using $K_{\mathrm{eff}}^{\mathrm{bulk}} = 18.7 \times 10^4$ erg/cm^3.
[b]Values calculated using $\langle d\rangle_{\mathrm{TEM}} = 8.3$ nm.
[c]Calculated using the experimental $M_S = 7.2-7.3$ emu/g values at $T = 250$ K.
[d]From Ref. 28.

C. In-field Mössbauer data

The reversal of the magnetic moment of single-domain particles is governed by the rate of flipping over an energy barrier that is proportional to the volume of the particle. This thermally activated process is described by a relaxation time τ that follows an Arrhenius law[35]

$$\tau = \tau_0 \exp\left(\frac{E_a}{k_B T}\right), \tag{4}$$

where E_a is the energy barrier for the magnetic reversion of the system, k_B is the Boltzmann constant, and τ_0 is the preexponential factor (of the order of $10^{-9}-10^{-13}$ s).[36,37] At room temperature ($T \gg T_B$) the relationship $\tau \ll \tau_L$ (where $\tau_L = 10^{-8}-10^{-9}$ s is the Larmor precession time of the nuclear magnetic moments[37]) is verified, so the fast relaxation makes the magnetic interactions to be averaged to zero and thus yields a paramagneticlike doublet. For temperatures below T_B (i.e., $\tau \gg \tau_L$), the Mössbauer spectrum is magnetically split. The hyperfine parameters at low temperature reported in Ref. 28 were in agreement with other reports on nanostructured magnetite[38,39] and showed no sizeable reduction of hyperfine fields, in contrast to other nanoparticle systems[40–43] where the reduction effect was assigned to surface disorder effects. From Eq. (4) it follows that the blocking temperature T_B depends on the experimental window time τ_M of a given measurement. It is well known that the ratio between the blocking temperatures from different techniques such as the Mössbauer and magnetization measurements (having typically $\tau_M = 10^{-8}$ and 10^2 s, respectively) inferred from Eq. (4) can be as large as $T_B^{\text{moss}}/T_B^{\text{mag}} \approx 10$. The blocking temperature for the Mössbauer experiments are usually defined as the temperature at which each of the blocked and SPM subspectra have 50% of the total spectral area. We estimated T_B^{Moss} from a series of Mössbauer spectra taken for 4.2 K $< T <$ 294 K (not shown) as being located somewhere between 110 and 120 K, which is about two to three times the value obtained from magnetization data.

In order to obtain local information of the rotational process of the magnetic moments, we performed the in-field Mössbauer measurements up to $B_{\text{app}} = 120$ kG. In this kind of experiments the effective field B_{eff} actually observed is the vectorial sum of B_{app} and the internal hyperfine fields B_{hyp}, $B_{\text{eff}} = B_{\text{hyp}} + B_{\text{app}}$ thus providing useful information about relative orientation between the local magnetic field at the probe nucleus and the external field (i.e., between B_{app} and the magnetic sublattices). Figure 5 shows the resulting Mössbauer spectra of sample ENDS at 4.2 K for $B_{\text{app}} = 0$, 10, 30, 50, 80, and 120 kG, applied along the γ ray direction. It can be seen from the figure that for increasing applied fields two distinct spectral components are apparently resolved. These two components originate from the ferromagnetic alignment of Fe atoms at A and B sites in the spinel structure, and the assignment of each subspectra to A and B sites (see Table III) is based on the zero-field spectrum.

It can be observed in Fig. 5 that the intensities of the second and fifth lines change as the applied field increases, which is a direct indication of the progressive reversal of the spins in the direction of the field. The spectral intensities of each line of a magnetically split spectrum are usually expressed as $3:x:1:1:x:3$, where x is the intensity of lines 2 or 5. For the present setup, the values of x span from $x=2$ for a randomly oriented system to $x=0$ for full alignment in the direction of the external field. More generally, the ratio of spectral areas (A_i) of lines 1 and 2 (or 5 and 6), can be related to the angle β between the magnetic quantization axis

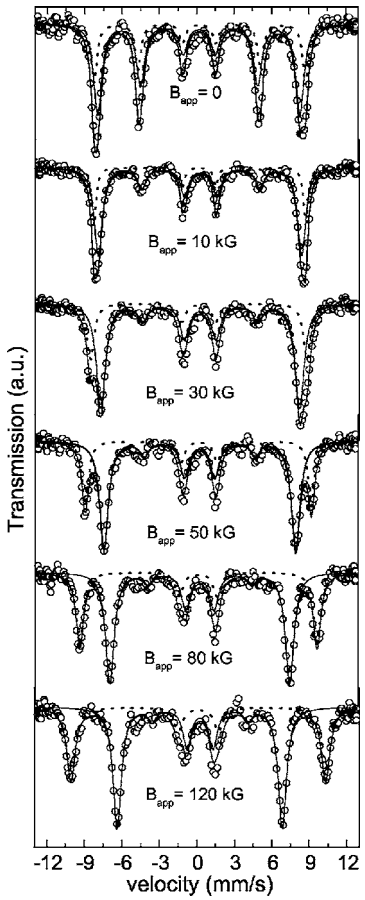

FIG. 5. Mössbauer spectra of sample ENDS at 4.2 K at different fields B_{app} applied along the γ-ray direction. Solid lines are the fitted experimental spectra (open circles), and dashed lines correspond to each component with the hyperfine parameters shown in Table III.

(assuming that the magnetic interaction is dominant) and the direction of the γ-ray beam (identical to the applied field B_{app} in our experimental setup) through the expression

$$\sin^2 \beta = \frac{6\Lambda}{4 + 3\Lambda}, \tag{5}$$

where $\Lambda = A_2/A_1$ (or A_5/A_6). The resulting values of Λ and β obtained from the fits at different fields are displayed in Table III. For $B_{\text{app}} = 0$ both subespectra could be fitted with the $\Lambda = 0.67$ value expected for a random powder. On the other side, we observed the different behavior for A and B sublattices under increasing applied fields. Indeed, Table III shows that the magnetic moments at A sites are already aligned for $B_{\text{app}} \geqslant 10$ kG, whereas the corresponding B-site moments show a gradual rotation and remain slightly misaligned up to the largest field of $B_{\text{app}} = 120$ kG. It is worthwhile to mention that the above observation relies on the capability of separately fitting (i.e., experimentally resolve) lines 2 and 5 of each subspectrum. These lines usually display strong overlap in ferrimagnetic materials, yielding unreliable Λ values from the fitting procedure. For the present data, we were able to resolve clearly lines 2 and 5 from each sublattice at $B_{\text{app}} = 120$ kG, using the obtained values of intensities as the starting free parameters for fitting at lower B_{app} values.

TABLE III. Hyperfine parameters at different applied fields B_{app}. B_{eff} is the effective field, I_T is the total intensity of each six-line subespectrum, Λ is the ratio of intensities of lines 2 and 1 (A_2/A_1), and β is the canting angle of each sublattice.

B_{app} (kG)	0		10		30		50		80		120	
Sites	*A*	*B*	*A*	*B*	*A*	*B*	*A*	*B*	*A*	*B*	*A*	*B*
B_{eff} (kG)	526(1)	508(1)	530(1)	505(1)	540(1)	496(1)	565(1)	479(1)	592(1)	449(1)	632(1)	411(1)
IS (mm/s)	0.18(1)	0.24(1)	0.17(1)	0.24(1)	0.15(1)	0.23(1)	0.18(1)	0.26(1)	0.13(1)	0.25(1)	0.13(1)	0.25(1)
QS (mm/s)	0.03(2)	−0.02(2)	0.03(2)	−0.03(2)	0.00(2)	−0.04(1)	0.01(1)	−0.04(2)	0.02(1)	−0.01(2)	−0.01(1)	−0.01(1)
Γ (mm/s)	0.63(3)	0.86(4)	0.45(4)	0.79(4)	0.69(4)	0.86(3)	0.62(4)	0.83(4)	0.70(4)	0.82(3)	0.75(4)	0.84(4)
I_T (%)	35(2)	65(2)	34(3)	66(2)	35(3)	65(2)	38(2)	62(3)	60(2)	40(3)	61(2)	39(3)
Λ	0.70(3)	0.68(3)	0.04(3)	0.23(3)	0.00(4)	0.16(4)	0.02(3)	0.13(3)	0.00(3)	0.09(3)	0.00(3)	0.10(3)
β[a] (degrees)			0(4)	34(4)	0(4)	31(4)	0(4)	31(4)	0(4)	22(4)	0(4)	22(4)

[a]Calculated from Eq. (5).

It is known that the ferromagnetic nanoparticles display noncollinear (canted) spin structure, although the location of these disordered spins (i.e., at the surface, core, or both) is still being discussed.[44–46] The actual spin structure is known to be more complex than the expected from the original Yafet-Kittel (YK) model of competing interactions,[47] and neutron diffraction and the Mössbauer studies have provided evidence that spin canting can be either restricted to a single magnetic sublattice or extended to both cation sites.[48–51] The present in-field Mössbauer data clearly show that magnetic moments at *A* sites (and also a fraction at *B* sites) are magnetically "soft," in agreement with the saturating behavior observed in $M(H)$ (see Fig. 4) at low temperatures. Additionally, the resolution of the two magnetic sublattices due to the application of a large external field makes possible to identify a minority of magnetically hard spins as located at *B* sites in the spinel structure. Despite their very high *local* anisotropy, however, this small fraction does not seem to contribute appreciably to the global magnetic anisotropy, as observed from the magnetization data presented before.

IV. DISCUSSION

The reduction of magnetic moments in small particles (1–10 nm) and thin films has been well documented along the last years[36,52] in both metallic and insulating materials.[32–34,38,42] A very-well accepted explanation for the reduction of M_S in ultrafine maghemite particles was given by Berkowitz *et al.*,[53] who proposed a shell-core structure with a magnetically dead surface layer originated from demagnetization of the (paramagnetic) surface spins. If the above mechanism is assumed for the present particles, a simple calculation using the bulk magnetization value (M_S^{bulk}=90 emu/g) would imply a core diameter $\langle d\rangle_{core}$ =2.5 nm and shell thickness t=2.9 nm. Such a thick paramagnetic surface layer, although not strictly unphysical, appears very unlikely since the Mössbauer spectra ruled out secondary Fe-containing phases, and CHNS compositional data showed that the organic material is much less than the necessary for such an organic coating. More recently, spin canting has been proposed[11,54,55] as the mechanism for the M_S reduction in spinel nanoparticles, due to competing interactions between sublattices that yield magnetic disorder at the particle surface.[56] Experimental evidence for this model has been found from the Mössbauer spectroscopy, and neutron diffraction measurements.[41,42,57] Extremely low values of M_S have been measured in ferrimagnetic spinel particles with $d \lesssim 15$ nm, attaining values as small as $\approx 0.06 M_S^{bulk}$, where M_S^{bulk} are the corresponding values of the bulk material.[56,58,59] From the theoretical side, Monte Carlo simulations using different models and approximations[54,55,60,61] have shown that the reduction of M_S is size dependent, and originates in a highly disordered spin surface with large magnetic anisotropy. The large magnetic anisotropy of the surface could be, in turn, responsible for the nonsaturating $M(H)$ curves even at large ($H \gtrsim 100$ kOe) applied fields, in agreement with the observed behavior of many spinel nanoparticles.[43,58,62,63]

For present Fe_3O_4 particles, however, the reduced M_S observed is not accompanied by the linear increase in $M(H)$ at high fields characteristic of canted systems. On the contrary, both the $M(H)$ curves and the in-field Mössbauer spectra at low temperature showed that the magnetic saturation is attained at moderate ($H \approx 10$ kOe) fields. We are therefore induced to hypothesize that, instead a thick spin-disordered surface layer, the origin for the observed reduction in M_S could be related to internal compensation of the magnetic sublattices *A* and *B* in the spinel structure. Further support to this idea comes from the evolution of the relative intensities of the *A* and *B* subespectra for increasing fields; it can be seen from Table III that the intensity of the subespectrum assigned to *B* site increases at expenses of the *A* subespectrum. The mechanisms that originate this peculiar situation are not obvious, and further experiments should be done before an explanation can be given.

Turning now to the measured magnetic anisotropy of the present nanoparticles, we want to discuss the values extracted from different techniques involving different experimental conditions. It can be seen from Table II that the resulting values of E_a obtained from magnetization and the Mössbauer data are essentially coincident with the magnetocrystalline anisotropy of bulk Fe_3O_4. Indeed, this is a remarkable result since shape anisotropy is usually a major contribution to the average total anisotropy.[64] It is generally accepted that, when the size of a magnetic particle decreases, surface effects become increasingly important. However, symmetry arguments suggest that the contribution from the surface should average to zero for a perfectly spherical particle.[40] Moreover, numerical calculations have shown[65]

that for an unstrained simple cubic lattice the bulk anisotropy vanishes in first order, whereas the contribution from the Néel surface anisotropy is second order, having the same cubic symmetry of the bulk. Therefore for highly symmetric particle shapes such as cubic or spherical, the contribution from both core and surface anisotropies should be comparable to the bulk magnetocrystalline values. These symmetry arguments are clearly applicable to our samples since, as mentioned above, the low magnetic anisotropy values obtained for these particles indicate magnetocrystalline anisotropy as the major contribution, setting an upper limit (no more than $\sim 2\%$) for possible deviations from sphericity.[64] Similar arguments can be applied to the case of cubic-shaped particles such as the faceted ones observed in our TEM images, since demagnetizing factors for a rectangular prism are within 15% of those of an ellipsoid having the same $a=b$, c, and $r=c/a$ parameters, as calculated by Aharoni.[66] Therefore, the above results support a picture of particles with spherical or edge-rounded cubic shapes, having cubic crystal structure with bulklike anisotropy.

A third value for E_a/k_B was previously[28] estimated from the low temperature Mössbauer data, using the model of collective magnetic excitations (CME).[67] In this model, small-angle fluctuations of the magnetic moments around the easy magnetization axis, with characteristic times much shorter than the Mössbauer sensing time τ_L, yield a decrease of the observed magnetic hyperfine field $B_{\text{eff}}(T)$ of the Mössbauer spectra.[37] Expressing the magnetic energy $E=E(\alpha_x,\alpha_y,\alpha_z)$ of a single particle as a function of the direction cosines $(\alpha_x,\alpha_y,\alpha_z)$ of the saturation magnetization M_S relative to the crystallographic axes, the thermal dependence of B_{eff} derived for an arbitrary function of the energy can be expressed as[68]

$$B_{\text{eff}}(T) = B_0\left(1 - \frac{k_B T}{\kappa V}\right), \tag{6}$$

where B_0 is the hyperfine field at $T=0$, and the effective anisotropy constant κ is given by

$$\frac{1}{\kappa} = 1 - \frac{1}{2}\left[\left(\frac{\partial^2 E}{\partial \alpha_x^2}\right)^{-1} + \left(\frac{\partial^2 E}{\partial \alpha_y^2}\right)^{-1}\right]. \tag{7}$$

In a previous work on Fe_3O_4 particles[38] with median sizes $\langle d\rangle$ ranging from 150 to 5 nm, it was reported that for $\langle d\rangle \leqslant 50$ nm no evidence of the Verwey transition is observed, suggesting that those particles preserve the cubic phase at low temperatures ($T<T_V$). Therefore, for the present nanometric Fe_3O_4 particles the values of magnetocrystalline anisotropy constants K_1 and K_2 of the high-temperature cubic phase with easy magnetization axis [111] should be used at any temperature. Applying these considerations and Eq. (7) an effective anisotropy constant $\kappa = -\frac{4}{3}(K_1+K_2/3)$ is obtained. Using the $\langle d\rangle_{\text{TEM}}$ value from the log-normal fit to the TEM distribution, the best fit of $B_{\text{eff}}(T)$ gave an effective anisotropy $\kappa = 24.3\times 10^4$ erg/cm^3, in good agreement with the 18.7×10^4 erg/cm^3 expected using the bulk magnetocrystalline values K_1 and K_2.

Inasmuch as the collective magnetic excitation model refers to the thermal excitations of the lowest energy levels, for $T \ll T_B$, the E_a parameter obtained from Eq. (6), using the CME model at zero field, gives information about single-particle anisotropy properties since interparticle interactions will have negligible effects on the detailed shape of the $E_a(\theta,H)$ surface in the vicinity and at the points of minima. On the other side, the values extracted from the frequency-dependent maxima in ac susceptibility data are related to the overcome of the magnetic anisotropy when thermal energy equals the average height of the energy barriers. The resulting E_a values extracted from the unblocking process can therefore be influenced by other contributions (e.g., interparticle interactions) that affect the values of the $E_a(\theta,H)$ surface near the maxima.[62]

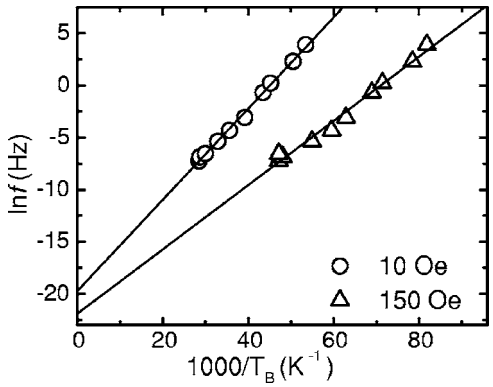

FIG. 6. $T_B(\ln f,H)$ dependence extracted from $\chi(f,T,H)$ data taken with $H=10$ and 150 Oe. The solid lines represent the best fit with Eq. (4).

In order to experimentally check the influence of small applied fields to the energy barriers, we measured the field dependence of T_B through ac susceptibility curves $\chi(f,T,H)$ at different applied dc fields. From the $\chi(f,T,H)$ data taken with $H=10$ and 150 Oe, we extracted the $T_B(f,H)$ dependences shown in Fig. 6. It can be observed that the frequency dependence $T_B(\ln f)$ is linear for both applied fields, demonstrating that the thermal activation mechanism of the blocking transition is preserved. The best fits of $T_B^{-1}(\ln f)$ data were obtained with $E_a/k_B = 436(9)$ and 296(15) K for $H=10$ and 150 Oe, respectively, indicating that the effect of the applied field is to decrease the effective anisotropy barrier $E_a(H)$. These results give support to the idea that the application of small fields can perturb the relative values and position of the maxima of the anisotropy energy function.

To further verify the above statements on a quantitative basis, we calculated the energy curves for a single particle in applied fields $H=0$, 10, and 150 Oe by the following relation

$$E(\theta,H) = K_{\text{eff}}V + \mu_0 HM\cos\theta, \tag{8}$$

where θ is the angle between the easy magnetization axis and the magnetization vector M of the particle, and H is the external field, applied along the easy axis of magnetization. In the presence of a small applied field H parallel to the easy direction of the particle (assumed here to be uniaxial), the energies at the minima for $\theta=0^\circ$ and $\theta=180^\circ$ will shift, and the transition probabilities between the two minima will result in different relaxation times τ_+ and τ_- (i.e., for forward and backwards relaxation processes, respectively). In the present case of modest applied fields, the observed relaxation times can be expressed as[35]

$$\frac{1}{\tau} = \frac{1}{\tau_-} + \frac{1}{\tau_+}, \tag{9}$$

with

$$\tau_\pm = \tau_0 \exp[E(\pm H)/k_B T]. \tag{10}$$

The energy curve for $H=150$ Oe was computed using a gradient method to calculate the local energy minima for each spin configuration along the magnetic energy surface $E(\theta,H)$. Using Eqs. (8)–(10) and considering the experimental *values* $M_S=12$ emu/g, $\langle d\rangle_{\mathrm{TEM}}=8.3$ nm and $E_a=K_{\mathrm{eff}}V=7.26\times10^{-14}$ erg the resulting height for the energy barrier $\Delta E/k_B=E_{\theta=90}/k_B-E_{\theta=0}/k_B$ was 500 K at $T=10$ K, in excellent agreement with the experimental results in Table II. A systematic series of computation for increasing applied fields H from 0 to 300 Oe showed that the difference ΔE_0 between the energy maximum and the minimum at $\theta=0$ goes deeper whereas the corresponding ΔE_π (minimum at $\theta=\pi$) gets shallower. Therefore, the corresponding relaxation times τ_+ and τ_- show opposite behavior for increasing fields H provided that $\mu_0 HM \ll K_{\mathrm{eff}}V$. We also computed the ratio τ_+/τ_- for our experimental conditions. The results obtained for $T=10$ K and the experimental applied fields $H=10$ and 150 Oe (see Fig. 6) yielded $\tau_+/\tau_-=2\times10^{-1}$ and 7×10^{-5}, respectively. These results give quantitative support to the assumption that the energy barriers (i.e., the whole relaxation process) can be changed in the observed amounts by the small fields used in our measurements. It should be pointed out that an exact calculation of the relaxation time would require, within Brown's model, to work with a probability function of angles and time, which obeys a Fokker-Planck equation. For symmetries different than uniaxial, the corresponding eigenvalues of the Fokker-Planck equation have been obtained[36] by numerical methods only for asymptotical situations (i.e., $k_BT/KV\to\infty$ or $k_BT/KV\to0$) not applicable to our present case.

It was already mentioned that the values of T_B obtained from the extrapolation of $H_C(T)\to0$ from $M(H)$ curves at low temperature differ from the ones obtained from ZFC measurements. The difference between these two results is probably related to the different field regimes in both techniques: while the ZFC maxima are obtained at low fields (typically 100 Oe), from a *previously* demagnetized state, the $H_C(T_B)$ is obtained after magnetic saturation of the samples (we used $H_{\mathrm{max}}=30$ kOe). Therefore, the moderate fields H_C applied when magnetization reversal takes place are likely to assist the unblocking process by decreasing the energy barriers and the inferred T_B will be lower than the corresponding values extracted from the ZFC curves measured at lower fields. The latter values, in turn, are mainly determined by the dynamics of the unblocking process that depends on the local minima at the energy surface originated from interparticle interactions. The above interpretation is in agreement with our estimations of the energy barriers E_a/k_B from ac susceptibility measured at low field,[28] (reproduced in Table II for clarity) which are larger than those extracted from the $H_C(T)$ fit.

During the analysis of the present data, the activation energies values extracted from $\chi(f,T,H)$ data with $H=0$ and 150 Oe were compared to the previously reported value[27] of $E_a=694$ K for the same END1 sample, obtained with $H=30$ Oe (see Table II). Contrary to the expected, the value obtained at an intermediate dc field is *larger* than the two obtained at lower and higher fields. Having verified that the temperatures of the maxima in our $\chi(f,T)$ curves were reproducible within $\Delta T\leqslant3$ K on different experimental runs, we attempted to investigate this seemingly nonmonotonic behavior of the anisotropy energy barriers by measuring the dependence $T_B(H)$ from ZFC curves at different fields. The results are shown in Fig. 7. It can be seen that for sample END1 there is a continuous increasing of $T_B(H)$ for decreasing fields, but a clear bending of T_B towards smaller values is observed for $H\leqslant20$ Oe. The reproducibility of these maxima in $M(T,H)$ curves was checked by performing a second set of ZFC curves, after allowing the sample to demagnetize at room temperature for several weeks. The results of the second run, plotted in Fig. 7 (black dots) demonstrate that the main features of the $T_B(H)$ curve obtained on the second run remain unaltered. This "reentrant" behavior has been originally found in a rather different context, i.e., in CuMn and GdAl spin glasses, and interpreted as due to the existence of a finite transition temperature at zero field.[69] Theoretical evidence of reentrant behavior of the Gabay-Tolouse line has been also found using a classical m-vector model with uniaxial anisotropy.[70]

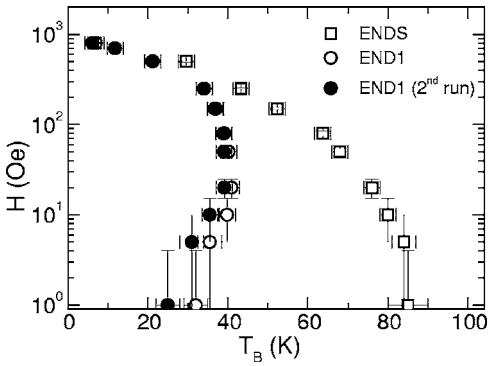

FIG. 7. The dependence $T_B(H)$ from ZFC curves of samples ENDS and END1 (first and second run) at different fields.

It seems more plausible, however, to relate this nonmonotonic field dependence of $T_B(H)$ at low fields with changes in the anisotropy energy surface $E(\theta,H)$. It can be seen from Fig. 7 that the $T_B(H)$ curves tend to merge each other in the large ($\geqslant500$ Oe) region, in agreement with the erasing of local minima by the external field, and both curves steadily diverge for small applied fields. However, for the concentrated sample a monotonic behavior persists down to the smallest applied fields. This behavior has been already found in diluted magnetite-based ferrofluids with different concentrations,[71] but no explanation for the nonmonotonic $T_B(H)$ dependence was offered. In a detailed work, Sappey *et al.*[72] proposed that the applied field can produce a small broadening of the energy barrier distribution, which suffices to give the observed field dependence of T_B. For the present data, different behavior is observed in two samples with identical particle size distributions but different average particle distances. A rough estimation using the compositional

data from Table I and $\langle d\rangle_{\mathrm{TEM}}=8.3$ nm, yielded values of the average particle-particle distance $\langle e\rangle=63$ nm and $\langle e\rangle=2$ nm for END1 and ENDS, respectively. Therefore in sample END1 we have $\langle e\rangle\approx 8\langle d\rangle$ and dipolar interactions are likely to be much weaker than for the $\langle e\rangle\approx\langle d\rangle/4$ situation of concentrated ENDS sample. The above arguments support the idea that the observed differences in $T_B(H)$ curves are related to the influence of interparticle interactions on the energy barrier. The absence of nonmonotonic behavior in the concentrated sample indicates that the local dipolar field must be included when considering the influence of the applied field on the barrier distribution, as proposed by Sappey *et al.*[72] Whatever the actual mechanism of the observed behavior of $T_B(H)$, the values of E_a in Table II obtained at $H=10$, 30, and 150 Oe can be understood as having the same origin.

In conclusion, our present results on nanometer-sized magnetite nanoparticles showed some intriguing facets. Single-particle anisotropy energy both in blocked and SPM regimes and different experimental time windows, indicates a reduced magnetization with minimum spin disorder. The magnetic response of the system can be described as bulklike (regarding magnetic softness and anisotropy) and, together with the reduced M_S and the magnetic saturation in moderate fields experimentally observed, can be explained if a change in each sublattice magnetization is assumed. This in turn might be originated from departures from the bulk populations of the Fe^{2+} and Fe^{3+} ions at A and B sites yielding a more complex magnetic configuration than the two-sublattice structure. At low fields, particle interactions become increasingly relevant, and may erase the nonmonotonic dependence of the blocking process observed in diluted samples. As the energy barrier height and distribution usually determine the dynamics of magnetic nanoparticle systems at low fields, its complex dependence with external parameters has to be solved before accurate parameters can be extracted from magnetic measurements.

ACKNOWLEDGMENTS

The authors are indebted to Prof. R.F. Jardim for his suggestion of exploring the field-dependence of the ac susceptibility, and Prof. A. Labarta for suggestions and critical reading of the manuscript. Thanks to Dr. A.B. Garcia for the compositional analysis. One of the authors (E.L.J.) acknowledges financial support from the VolkswagenStiftung, Germany, through a Postdoctoral Fellowship. This work was supported in part by Brazilian agencies FAPESP and CNPq.

[1] J. Smit and H. P. J. Wijin, *Ferrites: Physical Properties of Ferrimagnetic Oxides in Relation to Their Technical Applications* (Philips' Technical Library, Eindhoven, The Netherlands, 1959).
[2] I. Hilger, K. Frühauf, W. Andrä, R. Hiergeist, R. Hergt, and W. A. Kaiser, Acad. Radiol. **9**, 198 (2002).
[3] M. C. Bautista, O. Bomati-Miguel, X. Zhao, M. P. Morales, T. González-Carreño, R. Pérez de Alejo, J. Ruiz-Cabello, and S. Veintemillas-Verdaguer, Nanotechnology **15**, S154 (2004).
[4] S. H. Koenig, K. E. Kellar, D. K. Fujii, W. H. H. Gunther, K. Briley-Sæbø, and M. Spiller, Acad. Radiol. **9**, S5 (2002).
[5] M. Shinkai, J. Biosci. Bioeng. **94**, 606 (2002).
[6] V. Skumryev, S. Stoyanov, Y. Zhang, G. Hadjipanayis, D. Givord, and J. Nogués, Nature (London) **423**, 850 (2003).
[7] M. Jamet, W. Wernsdorfer, C. Thirion, D. Mailly, V. Dupuis, P. Mélinon, and A. Pérez, Phys. Rev. Lett. **86**, 4676 (2001).
[8] F. Luis, F. Petroff, J. M. Torres, L. M. Garcia, J. Bartolomé, J. Carrey, and A. Vaurès, Phys. Rev. Lett. **88**, 217205 (2002); See also the comment by M. F. Hansen and S. Mørup, *ibid.* **90**, 059705 (2003); and the reply by F. Luis *et al.*, *ibid.* **90**, 059706 (2003).
[9] E. C. Stoner and E. P. Wohlfarth, Philos. Trans. R. Soc. London, Ser. A **240**, 599 (1948).
[10] M. F. Hansen, C. B. Koch, and S. Mørup, Phys. Rev. B **62**, 1124 (2000).
[11] O. Iglesias and A. Labarta, Physica B **343**, 286 (2004).
[12] S. Mørup, M. B. Madsen, J. Franck, J. Villadsen, and C. J. W. Koch, J. Magn. Magn. Mater. **40**, 163 (1983).
[13] G. Ennas, A. Falqui, S. Marras, C. Sangregorio, and G. Marongiu, Chem. Mater. **16**, 5659 (2004).
[14] L. A. Harris, J. D. Goff, A. Y. Carmichael, J. S. Riffle, J. J. Harburn, T. G. St. Pierre, and M. Saunders, Chem. Mater. **15**, 1367 (2003).
[15] R. Skomski, J. Phys.: Condens. Matter **15**, R841 (2003).
[16] I. Leonov, A. N. Yaresko, V. N. Antonov, M. A. Korotin, and V. I. Anisimov, Phys. Rev. Lett. **93**, 146404 (2004).
[17] Z. Kakol and J. M. Honig, Phys. Rev. B **40**, 9090 (1989).
[18] R. Aragon, Phys. Rev. B **46**, 5334 (1992).
[19] E. J. W. Verwey, Nature (London) **144**, 327 (1939).
[20] M. Ziese, Rep. Prog. Phys. **65**, 143 (2002).
[21] J. P. Wright, J. P. Attfield, and P. G. Radaelli, Phys. Rev. B **66**, 214422 (2002).
[22] M. Iizumi, T. F. Koetzle, G. Shirane, S. Chikazumi, M. Matsui, and S. Todo, Acta Crystallogr., Sect. B: Struct. Crystallogr. Cryst. Chem. **B38**, 2121 (1982).
[23] F. Walz, J. Phys.: Condens. Matter **14**, R285 (2002).
[24] K. Abe, Y. Miyamoto, and S. Chikazumi, J. Phys. Soc. Jpn. **41** (1976) 1894.
[25] W. Palmer, Phys. Rev. **131**, 1057 (1963).
[26] W. Hundt, R. Petsch, T. Helmberger, and M. Reiser, Eur. Radiol. **10**, 1495 (2000).
[27] L. F. Gamarra, G. E. S. Brito, W. M. Pontuschka, E. Amaro, A. H. C. Parma, and G. F. Goya, J. Magn. Magn. Mater. **289**, 439 (2005).
[28] A. D. Arelaro, A. L. Brandl, E. Lima, Jr., and G. F. Goya, J. Appl. Phys. **97**, 10J316 (2005).
[29] An error in Ref. 27 was brought into our attention: The $M(H)$ cycle shown in the inset of Fig. 2 of that reference corresponds to FFMAG particles obtained from a sol-gel route, not to the ENDOREM™ particles as stated in the caption.
[30] E. F. Ferrari, F. C. S. da Silva, and M. Knobel, Phys. Rev. B **56**, 6086 (1997).
[31] B. D. Cullity, *Introduction to Magnetic Materials* (Addison-Wesley, Reading, MA 1972).
[32] A. E. Berkowitz, J. A. Lahut, I. S. Jacobs, L. M. Levinson, and D. W. Forester, Phys. Rev. Lett. **34**, 594 (1975).
[33] R. H. Kodama, S. A. Makhlouf, and A. E. Berkowitz, Phys. Rev. Lett. **79**, 1393 (1997).
[34] S. A. Oliver, H. H. Hamdeh, and J. C. Ho, Phys. Rev. B **60**, 3400 (1999).
[35] W. F. Brown, Jr., Phys. Rev. **130**, 1677 (1963).
[36] J. L. Dormann, D. Fiorani, and E. Tronc, Adv. Chem. Phys. **98**, 283 (1997).
[37] S. Mørup, Hyperfine Interact. **60**, 959 (1990).
[38] G. F. Goya, T. S. Berquo, F. C. Fonseca, and M. P. Morales, J. Appl. Phys. **94**, 3520 (2003).
[39] P. Tartaj, M. P. Morales, S. Veintemillas-Verdaguer, T. González-Carreño, and C. J. Serna, J. Phys. D **36**, R182 (2003).
[40] F. Bødker, S. Mørup, and S. Linderoth, Phys. Rev. Lett. **72**, 282 (1994).
[41] C. J. Serna, F. Bødker, S. Mørup, M. P. Morales, F. Sandiumeng, and S. Veintemillas-Verdaguer, Solid State Commun. **118**, 437 (2201).
[42] J. Z. Jiang, G. F. Goya, and H. R. Rechenberg, J. Phys.: Condens. Matter **11**, 4063 (1999).
[43] G. F. Goya, H. R. Rechenberg, and J. Z. Jiang, J. Appl. Phys. **84**, 1101 (1998).
[44] V. Sepelak, D. Baabe, F. J. Litterst, and K. D. Becker, Hyperfine Interact. **126**, 143 (2000).

[45]C. N. Chinnasamy *et al.*, Phys. Rev. B **63**, 184108 (2001).
[46]S. Mørup, J. Magn. Magn. Mater. **266**, 110 (2003).
[47]Y. Yafet and C. Kittel, Phys. Rev. **87**, 290 (1952).
[48]E. Tronc *et al.*, J. Magn. Magn. Mater. **221**, 63 (2000).
[49]G. F. Goya and E. R. Leite, J. Phys.: Condens. Matter **15**, 641 (2003).
[50]C. N. Chinnasamy, A. Narayanasamy, N. Ponpandian, K. Chattopadhyay, H. Guérault, and J-M Greneche, J. Phys.: Condens. Matter **12**, 7795 (2000).
[51]S. A. Oliver, H. H. Hamdeh, and J. C. Ho, Phys. Rev. B **60**, 3400 (1999).
[52]X. Batlle and A. Labarta, J. Phys. D **35**, R15 (2002).
[53]A. E. Berkowitz, W. J. Schuele, and P. J. Flanders, J. Appl. Phys. **39**, 1261 (1968).
[54]H. Kachkachi and M. Dimian, Phys. Rev. B **66**, 174419 (2002).
[55]O. Iglesias and A. Labarta, Phys. Rev. B **63**, 184416 (2001).
[56]R. H. Kodama, A. E. Berkowitz, E. J. McNiff, and S. Foner, Phys. Rev. Lett. **77**, 394 (1996).
[57]D. Lin, A. C. Numes, C. F. Majkrzak, and A. E. Berkowitz, J. Magn. Magn. Mater. **145**, 343 (1995).
[58]B. Martínez, X. Obradors, Ll. Balcells, A. Rouanet, and C. Monty, Phys. Rev. Lett. **80**, 181 (1998).
[59]T. Lutz, C. Estouvnès, and J. L. Guille, J. Sol-Gel Sci. Technol. **13**, 929 (1998).
[60]K. N. Trohidou and J. A. Blackman, Phys. Rev. B **41**, 9345 (1990).
[61]H. Kachkachi, A. Ezzir, M. Nogués, and E. Tronc, Eur. Phys. J. B **14**, 681 (2000).
[62]R. H. Kodama and A. E. Berkowitz, Phys. Rev. B **59**, 6321 (1999).
[63]G. F. Goya, Solid State Commun. **130**, 783 (2004).
[64]For instance, deviations from ideal spherical shape into a prolate spheroid with $r=c/a$ ($a=b$ and c are the minor and major axis, respectively) will add to the effective anisotropy through a shape-anisotropy constant given by $K_S=\pi M^2[1-(3/B^2)([r\ln(r+B)]/B-1)]$, where M is the particle magnetization and $B=\sqrt{r^2-1}$. Since shape anisotropy is proportional to M^2, a ratio r as small as 1.3 will contribute with $K_{shape}\sim 14\times 10^4$ erg/cm^3, which is about the same value of the bulk magnetocrystalline anisotropy.
[65]D. A. Garanin and H. Kachkachi, Phys. Rev. Lett. **90**, 065504 (2003).
[66]A. Aharoni, J. Appl. Phys. **83**, 3432 (1998).
[67]S. Mørup, J. A. Dumesic and H. Topsøe, in *Applications of Mössbauer Spectroscopy*, edited by R. L. Cohen (Academic, New York, 1980), Vol. 2.
[68]S. Mørup, J. Magn. Magn. Mater. **37**, 39 (1983).
[69]B. Barbara and A. P. Malozemoff, J. Less-Common Met. **94**, 45 (1983).
[70]S. R. Vieira, F. D. Nobre, and F. A. da Costa, J. Magn. Magn. Mater. **210**, 390 (2000).
[71]W. Luo, S. R. Nagel, T. F. Rosenbaum, and R. E. Rosensweig, Phys. Rev. Lett. **67**, 2721 (1991).
[72]R. Sappey, E. Vincent, N. Hadacek, F. Chaput, J. P. Boilot, and D. Zins, Phys. Rev. B **56**, 14551 (1997).